Molecular Diversity
https://doi.org/10.1007/s11030-021-10229-z

ORIGINAL ARTICLE

Synthesis of new 2-aminothiazolyl/benzothiazolyl-based 3,4-dihydropyrimidinones and evaluation of their effects on adenocarcinoma gastric cell migration

Mohsen Sagha[1] · Fatemeh Mousaei[2] · Mahtab Salahi[2] · Nima Razzaghi-Asl[3]

Received: 1 March 2021 / Accepted: 27 April 2021

Abstract

Gastric cancer is one of the malignant tumors of the gastrointestinal tract that, despite its decrease in recent years, is still the fourth most common cancer and the second leading cause of cancer-related death. Various strategies including chemotherapy are used to keep cancer cells from spreading and induce apoptotic death in them. Recent studies have shown that dihydropyrimidinones (DHPMs) are privileged structures in medicinal chemistry due to their pharmacological effects. A number of new 2-aminothiazolyl/benzothiazolyl derivatives of 3,4-DHPMs (**3**–**8**) were synthesized and structurally identified, and then their effects on the migration behavior of human AGS cells (gastric cancer cells) were investigated. Molecular docking and molecular dynamics (MD) simulations were applied to explore binding potential and realistic binding model of the assessed derivatives through identification of key amino acid residues within L5/α2/α3 allosteric site of kinesin 5 (Eg5) as a validated microtubule-dependent target for monastrol as a privileged DHPM derivative.

Graphical abstract

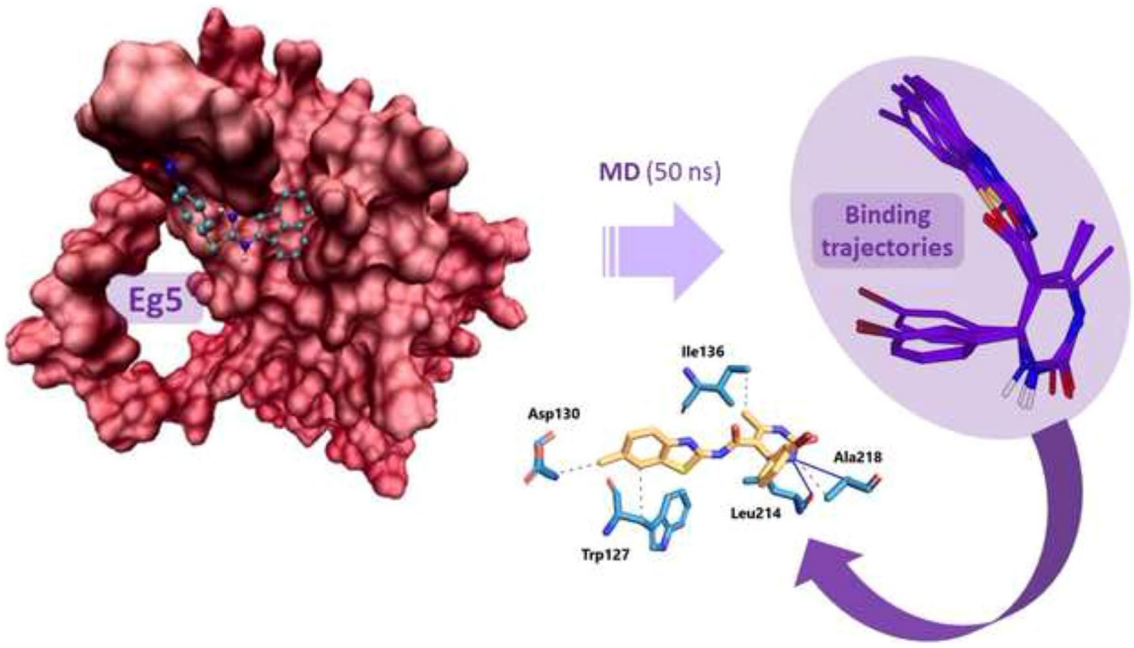

Keywords Gastric cancer · 3,4-Dihydropyrimidinones · Cell migration

Extended author information available on the last page of the article

Published online: 29 May 2021

Introduction

Cancer refers to a family of diseases characterized with uncontrolled growth of cells that are able to spread out to other parts of the body [1]. Cancers can originate from environmental and hereditary causes. Eating habits, lack of physical activity, alcohol consumption, smoking and infection play an important role in causing cancer [2]. Gastric cancer is one of the malignant tumors of the gastrointestinal tract that, despite its decreasing rate in recent years, is still the fifth incidence and third mortality worldwide [3, 4].

Cell migration plays an important role in the spread of cancer cells, tissue invasion and metastasis, which is the leading cause of death in cancer patients. Metastasis is a complex pathological phenomenon in which the cancer cells with epithelial origin transit from the epithelial state to the mesenchymal phenotype, a process that is called EMT and propagate from the site of the primary tumor to invade a location other than the site of the primary tumor [5]. There have been many advances in the treatment of gastric cancer recently, but the treatment of gastric cancer still remains an important challenge [6]. Therefore, it is necessary to seek appropriate and promising strategies for the treatment of gastric cancer. So, the design and development of compounds that are able to prevent cancer cells from spreading and migrating from one tissue to another (metastasis) are of particular interest for the treatment of advanced stages of cancer.

Among different chemical compounds indicating the cytotoxic effects on cancer cells, dihydropyrimidinones (DHPM) are important heterocyclic compounds in medicinal chemistry due to their diverse pharmacological effects [7, 8]. One of the most important and first compounds of dihydropyrimidones that proved to have the anticancer effects is monastrol (Fig. 1), which specifically prevents metastasis through inhibiting the movement of kinesin spindle protein known as Eg5 protein on microtubule [9]. It has been revealed that monastrol disrupts cell cycle through allosteric inhibition of microtubule-stimulated ADP release from Eg5 followed by apoptotic signaling pathway leading to cell death.

Eg5 is a mitotic kinesin that provides proper formation of a bipolar mitotic spindle during mitosis, through ATP hydrolysis [10], and as mentioned above, dihydropyrimidine derivatives are foremost representative chemotypes for inhibiting Eg5 that bind to the allosteric L5 binding site in the motor domain, which is an ATP non-competitive site of action [11, 12]. It should be also emphasized that one of the advantageous features of dihydropyrimidinones with regard to Eg5 is their selective binding pattern to this kinesin [13].

Besides dihydropyrimidinone derivatives, a variety of structurally diverse Eg5 inhibitors such as thiazoles and

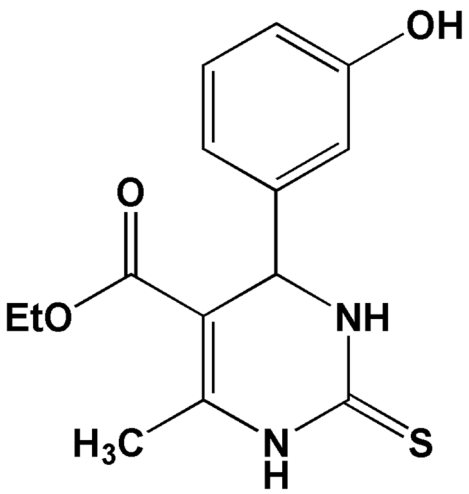

Fig. 1 Chemical structure of monastrol

their derivatives as important cytotoxic and anticancer agents were reported in the literature to act via allosteric binding mechanism [14, 15]. In the current study, with the aim of incorporating thiazole moiety and its more hydrophobic analogue, i.e., benzothiazole into the monastrol-derived 3,5-disubstituted dihydropyrimidine structures as validated Eg5 inhibitors, a number of new 2-amino-6-methylbenzothiazolyl 3,4-dihydropyrimidinone (**3**–**5**) and 2-aminothiazolyl 3,4-dihydropyrimidinone (**6**–**8**) derivatives were synthesized and structurally identified to evaluate their effects on the migratory behavior of human gastric cancer cells. Subsequently; binding ability of assessed compounds within L5/α2/α3 allosteric site of kinesin 5 (Eg5) as a validated microtubule associated target for DHPMs was explored through molecular docking and molecular dynamics simulations. It was interesting to note that improved polar interactions were probably driving force for re-orientation of compound **4** in the binding site of Eg5 to achieve more stable binding mode.

Materials and methods

Chemistry

All materials and reagents were purchased from Sigma-Aldrich (India) company and used without further purification. Melting points were determined using an Electro thermal type 9200 MP apparatus (England) and uncorrected. Infra-Red (IR) spectra were obtained by a Perkin Elmer-400 FT-IR spectrophotometer (England). Proton nuclear magnetic resonance (^{1}H-NMR) spectra were recorded on a Bruker DRX400 spectrometer (400 MHz). Mass (MS) spectra were reported by an Agilent 7890A spectrometer (USA).

General procedure for the synthesis of N-(6-methylbenzo[d] thiazole-2-yl)-3-oxo butane amide (1) and N-(thiazole-2-yl)-3-oxo butane amide (2)

8 mmol of 2-amino-6-methyl benzothiazole or 2-aminothiazole was dissolved in 10 mL xylene (148 °C) and 10 mmol 2,2,6-trimethyl-1,3-dioxin-4-one was added to the mixture. After 2 h reflux, the mixture was cooled to room temperature. Obtained precipitates were filtered and washed with petroleum ether (3 × 2 mL). Subsequent recrystallization from ethanol afforded the pure final product.

General procedure for the synthesis of 2-amino-6-methylbenzothiazole derivatives of 3,4-dihydropyrimidinones (3–5) and 2-aminothiazole derivatives of 3,4-dihydropyrimidinones (6–8)

For the synthesis of DHPM derivatives, 3.9 mmol N-(6-methylbenzo[d]thiazole-2-yl)-3-oxo butane amide or *N*-(thiazole-2-yl)-3-oxo butane amide, 3.6 mmol urea, 1 mL HCl, and 3 mmol corresponding aldehyde were mixed in 9 mL ethanol and refluxed for 24 h. After completion of the reaction (controlled by TLC), a mixture of water and ice cubes was added to the flask and stirred for 5 min. Obtained precipitates were filtered and washed with cold water (3 × 2 mL). Subsequent recrystallization from ethanol afforded the pure final products (40.6–51.9%).

Biological assessment

Reagents and chemicals

Fetal bovine serum (FBS), RPMI 1640, trypsin, and phosphate-buffered saline (PBS) were all obtained from Biosera (Ringmer, UK). 3-(4,5-Dimethylthiazol-2-yl)-2,5-diphenyltetrazolium bromide or MTT was purchased from Sigma (Saint Louis, MO, USA), and penicillin/streptomycin was purchased from Invitrogen (San Diego, CA, USA). Cisplatin and dimethyl sulfoxide (DMSO) were obtained from EBEWE Pharma (Unterach, Austria) and Merck (Darmstadt, Germany), respectively.

Evaluation of cytotoxicity by MTT assay

Cell viability following exposure to the synthetic compounds was estimated via MTT reduction assay [16]. AGS cells were plated in 96-well microplates at a density of 1×10^4 cells per well in RPMI 1640 medium supplemented with 10% FBS and 1% pen/strep for 24 h, and then, the culture medium was changed to a serum-free medium containing the desired volume of the synthetic compounds (which were firstly dissolved in DMSO and then diluted in medium). After 24 h of culture, the medium was removed and MTT was added to each well at a final concentration of 0.5 mg/mL, and the plates were incubated for another 4 h at 37 °C in a dark condition. Then, the resulted formazan crystals were solubilized in 200 µL DMSO and optical density was measured at 570 nm with background correction at 570 nm using a Bio-Rad microplate reader (Model 680, USA). Control wells contained no drugs, and blank wells contained only growth medium for background correction. The percentage of cell viability compared to the control wells was calculated for each concentration of the compounds, and IC_{50} values were calculated with SigmaPlot version 12.5. In all groups, the absorbance of wells containing no cells (Blank) was subtracted from the sample well absorbance.

Wound healing assay

To evaluate the cell migration property following treatment, AGS cells (6×10^4) were seeded onto 24-well plates to grow in a monolayer for 48 h. Then a sterile 100–200 µL pipette tip was held vertically to scratch a cross in each well. The detached cells were removed by washing with 500 µL PBS and shaking at 500 rpm for 5 min. Then, the IC_{50} concentrations of the compounds were prepared by dilution with serum-free medium. In the next step, the medium of the wells was removed and the first row of the plate was treated as control and the next rows were treated with IC_{50} concentrations. After 24 h, photographs with Olympus CKX41 inverted microscope were taken using Cellsens software, standard 1.14 connected to the DP27 camera [17, 18].

In silico studies

Molecular docking

Lamarckian genetic algorithm (LGA) incorporated into AutoDock4.2 package was used to run ligand flexible docking simulations on DHPM molecules [19, 20]. All the preprocessing ligand and receptor steps and docking parameters were arranged according to the previous protocols [21]. Post-docking analysis of ligand-enzyme interactions was performed by protein–ligand interaction profiler (PLIP) fully automated server [22]. Intended 3D structure of kinesin 5 (Eg5) in complex with fluorastrol (PDB code **2 × 7e**) was retrieved from Brookhaven Protein Bank (PDB) in the X-ray crystallographic format [23].

Molecular dynamics

The all-atom MD simulations were performed using GROMACS 5.1.1 computational package [24]. Topology files and other force field parameters for DHPM molecules were generated by PRODRG server [25]. Prior to energy minimization, water molecules were represented using a

simple point charge (SPC216) model and approximately 29,843 water molecules were added to the system. Overall charge neutrality of the complex system (Eg5, ligand, and water molecules) was ensured via insertion of appropriate amounts of counter-ions (4 Na^+ ions).

GROMOS96 43a1 was used as the force field for determination of all bonding and nonbonding interactions. Steepest descent followed by conjugate gradient algorithms was used for energy minimization of the protein–ligand complex. After energy minimization process, position restraint procedure was performed in association with NVT and NPT ensembles. An NVT ensemble was adopted at constant temperature of 300 K with a coupling constant of 0.1 ps and time duration of 500 ps. Subsequent to temperature stabilization, NPT ensemble was performed in a way that a constant pressure of 1 bar was employed with a coupling constant of 5.0 ps and time duration of 1000 ps. Pressure was maintained at 1 bar with the Parrinello-Rahman barostat [26]. The lincs algorithm for covalent bond constraints was applied [27]. The particle-mesh ewald (PME) and cut-off methods were used to treat the long-range electrostatic and van der Waals interactions, respectively [28]. All other bonding parameters were set due to our previous report [29], and 20 ns MD simulation was performed with monitoring of equilibration by examining the stability of the energy, temperature, and the density of the system as well as the root mean square deviations (RMSDs) of the backbone atoms.

Results and discussion

Chemistry

Chemical structures of DHPM derivatives were confirmed by spectroscopic methods. Spectroscopic results of synthesized compounds are illustrated below (Actual analytical data are given in Online Resource through supplementary material).

4-(3-Hydroxyphenyl)-6-methyl-N-(6-methylbenzo [d] thiazol-2-yl) -2-oxo-1,2,3,4-tetrahydropyrimidine-5-carboxamide (3)

White crystal, yield 40.6%; mp: 290–292 °C; IR (KBr) ν_{max} (cm^{-1}): 3357.1 (br, O–H phenol & N–H, amide), 3322.0 (N1-H, urea), 3209.4 (N3-H, urea), 1694.4 (C=O, amide), 1622.9 (C=O, urea); ^{1}H- NMR (400 MHz, DMSO-d6) δ (ppm) 11.83 (1H, brs, NH-amide), 9.42 (1H, brs, N1H-urea), 9.06 (1H, brs, OH-phenol), 7.75 (1H, brs, N3H-urea), 7.71 (1H, brs, C7′H-benzothiazole), 7.59 (1H, d, J = 8 Hz, C4′H-benzothiazole), 7.22 (1H, d, J = 7.2 Hz, C5′H-benzothiazole), 7.09 (1H, t, J = 8 Hz, CH-phenyl), 6.70–6.72 (2H, m, CH-phenyl), 6.62 (1H, d, J = 6.8 Hz, CH-phenyl), 5.54 (1H, brs, C4H-DHPM), 2.39 (3H, s, 6′-CH_3-benzothiazole), 2.17 (3H, s, 6′-CH_3-DHPM); MS m/z (%): 394 (0/9) [M^+], 189 (100),164 (23), 111 (64), 77 (9).

4-(3-Bromophenyl)-6-methyl-N-(6-methylbenzo [d] thiazol-2-yl) -2-oxo-1,2,3,4-tetrahydropyrimidine-5-carboxamide (4)

White crystal, yield 49.6%; mp: 262–264 °C; IR (KBr) ν_{max} (cm^{-1}): 3434.6 (N–H, amide), 3201.8 (N1-H, urea), 31980.3 (N3-H, urea), 1681.0 (C=O, amide), 1620.9 (C=O, urea), 693.4 (C–Br); ^{1}H NMR (DMSO-d6) δ (ppm) 11.83 (1H, brs, NH-amide), 9.16 (1H, brs, N1H-urea), 7.86 (1H, brs, N3H-urea), 7.59 (1H, d, J = 8.4 Hz, C4′H- benzothiazole), 7.46–7.48 (2H, m, CH-phenyl & C7′H-benzothiazole), 7.26–7.31 (3H, m, CH-phenyl & C5′H-benzothiazole), 7.01 (1H, d, J = 8.8 Hz, CH-phenyl), 5.56 (1H, brs, C4H-DHPM), 2.50 (3H, s, 6′-CH_3-benzothiazole), 2.20 (3H, s, 6′-CH_3-DHPM); MS m/z (%): 250 (28), 206 (52), 165 (46), 135 (21), 111 (100).

4-Phenyl-6-methyl-N-(6-methylbenzo [d] thiazol-2-yl) -2-oxo-1,2,3,4-tetrahydropyrimidine-5-carboxamide (5)

White crystal, yield 51.9%; mp: 268–271 °C; IR (KBr) ν_{max} (cm^{-1}): 3367.7 (N–H, amide), 3224.5 (N1-H, urea), 3113.9 (N3-H, urea), 1695.8 (C=O, amide), 1605.7 (C=O, urea); ^{1}H NMR (DMSO-d6) δ (ppm) 11.80 (1H, brs, NH-amide), 9.09 (1H, brs, N1H-urea), 7.96 (1H, brs, N3H-urea), 7.58 (1H, d, J = 8.4 Hz, C4′H- benzothiazole), 7.50 (1H, brs, C7′H-benzothiazole), 7.28–7.35 (5H, m, CH-phenyl), 7.01 (1H, d, J = 9.2 Hz, C5′H-benzothiazole), 5.59 (1H, brs, C4H-DHPM), 2.50 (3H, s, 6′-CH_3-benzothiazole), 2.18 (3H, s, 6′-CH_3-DHPM); MS m/z (%): 185 (24), 165 (100), 137 (15), 110 (9), 44 (15).

4-(4-Nitrophenyl)-6-methyl-N-(thiazol-2-yl)-2-oxo-1,2,3,4-tetrahydropyrimidine-5-carboxamide (6)

Pale yellow crystal, Yield 42.13%; mp: 268–270 °C; IR (KBr) ν_{max} (cm^{-1}): 3343.3 (N–H, amide), 3236.7 (N1-H, urea), 3127.3 (N3-H, urea), 1715.7 (C=O, amide), 1673.2 (C=O, urea), 1341.5 & 1537.6 (C–NO_2 aromatic); ^{1}H NMR (DMSO-d6) δ (ppm) 11.79 (1H, brs, NH-amide), 9.15 (1H, brs, N1H-urea), 8.22 (2H, d, J = 8.8 Hz, CH-phenyl), 7.91 (1H, brs, N3H-urea), 7.53 (2H, d, J = 8.8 Hz, CH-phenyl), 7.43 (1H, d, J = 3.2 Hz, C4H-thiazole), 7.14 (1H, brs, C5H-thiazole), 5.55 (1H, brs, C4H-DHPM), 2.16 (3H, s, 6′-CH_3-DHPM); MS m/z (%): 248 (53), 205 (34), 169 (100), 110 (11), 75 (4).

4-(4-Fluorophenyl)-6-methyl-N-(thiazol-2-yl)-2-oxo-1,2,3,4-tetrahydropyrimidine-5-carboxamide (7)

Pale yellow crystal, Yield 47.5, mp: 170–171 °C; IR (KBr) ν_{max} (cm^{-1}): 3398.2 (N–H, amide), 3226.7 (N1-H, urea), 3098.3 (N3-H, urea), 1704.0 (C=O, amide), 1667.6 (C=O, urea), 1232.8 (C-F); ^{1}H NMR (DMSO-d6) δ (ppm) 11.70 (1H, brs, NH-amide), 9.02 (1H, brs, N1H-urea), 7.74 (1H, brs, N3H-urea), 7.43 (1H, d, J = 3.2 Hz, C4H-thiazole), 7.31 (2H, d, J = 5.6 Hz, CH-phenyl), 7.28 (2H, d, J = 5.6 Hz, CH-phenyl), 7.13 (1H, brs, C5H-thiazole), 5.54 (1H, brs, C4H-DHPM), 2.14 (3H, s, 6′-CH_3-DHPM); MS *m/z* (%): 288 (24), 205 (100), 127 (25), 100 (19), 58 (16).

4-(4-Chlorophenyl)-6-methyl-N-(thiazol-2-yl)-2-oxo-1,2,3,4-tetrahydropyrimidine-5-carboxamide (8)

Pale yellow crystal, Yield: 51.5%; mp: 260–262 °C; IR (KBr) ν_{max} (cm^{-1}): 3265.5 (N–H, amide), 3203.2 (N1-H, urea), 3125.4 (N3-H, urea), 1709.2 (C=O, amide) 1683.9 (C=O, urea), 760.2 (C–Cl); ^{1}H NMR (DMSO-d6) δ (ppm) 11.72 (1H, brs, NH-amide), 9.04 (1H, brs, N1H-urea), 7.77 (1H, brs, N3H-urea), 7.43 (1H, d, J = 3.6 Hz, C4H-thiazole), 7.40 (2H, d, J = 8.4 Hz, CH-phenyl), 7.28 (2H, d, J = 7.4 Hz, CH-phenyl), 7.14 (1H, brs, C5H-thiazole), 5.53 (1H, brs, C4H-DHPM), 2.13 (3H, s, 6′-CH_3-DHPM); MS *m/z* (%): 249 (48), 169 (100), 137 (50), 111 (70), 75(15).

The first step of the synthetic rout included a nucleophilic attack of primary aromatic amine into dioxin reactant to afford 3-oxo butane amide intermediate (**1** & **2** in scheme 1). Subsequent stage involved nucleophilic attack of urea to corresponding aldehyde and then reaction with 3-oxo butane amide to give the final derivatives via cyclization and water removal (Scheme 1).

Biological assessment

Cytotoxicity assessment

Prepared DHPM derivatives were assessed for their cytotoxic effects on AGS cell line in terms of IC_{50} values. As shown in Table 1, compounds **7** with *para*-fluorophenyl moiety exhibited higher toxicity (IC_{50} 7.06 µg/ml) with regard to other compounds and the cytotoxic effects of DHPMs on AGS cell lines could be ordered as **7** > **6** > **8** > **5** > **4** > **3**. Results indicated that none of the assessed compounds could be as cytotoxic as *cis*-platin against AGS cell lines except compound **7**. Dose-dependent diagrams for compounds **5** and **7** in terms of cell survival are depicted in Fig. 2. We found that cell survival effect of **4** differed slightly from **3** only in low doses and not in high doses. Similar trend was observed for compounds **6** and **8**, but in the case of compound **7**, a curvature with steeper slope could be detected after 12.5 µg/ml doses (Fig. 2).

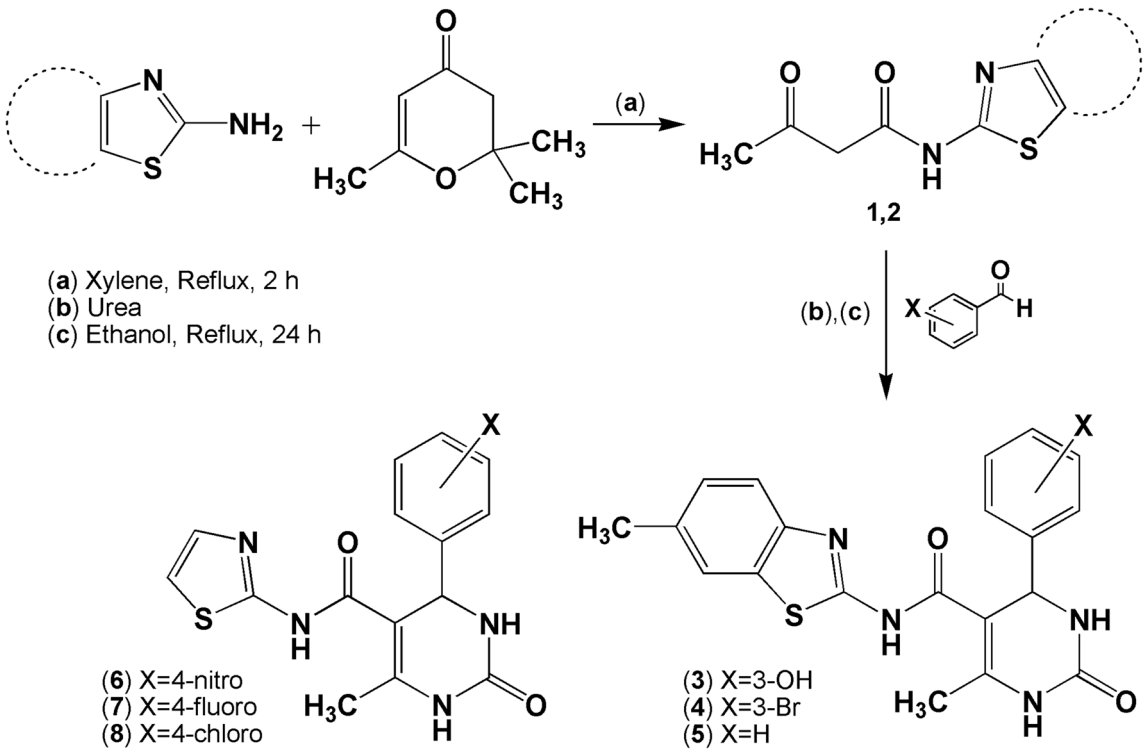

Scheme 1 Synthetic route toward dihydropyrimidinones

Table 1 IC_{50} values of DHPM derivatives vs assessed AGS cell line

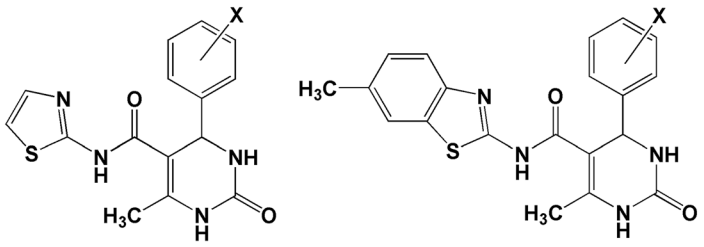

Compound	*X*	IC_{50} (μg/ml) ± SD	Consensus Log $P_{o/w}$ [a]
3	3-OH	42.73 ± 1.35	2.39
4	3-Br	38.34 ± 1.43	3.38
5	H	21.70 ± 1.19	2.79
6	4-NO_2	19.60 ± 0.76	0.65
7	4-F	7. 60 ± 0.61	1.68
8	4-Cl	21.50 ± 2.01	1.90
Cis-platin	–	11.49 ± 1.35	–

[a]Data were estimated via SwissADME webserver [31]

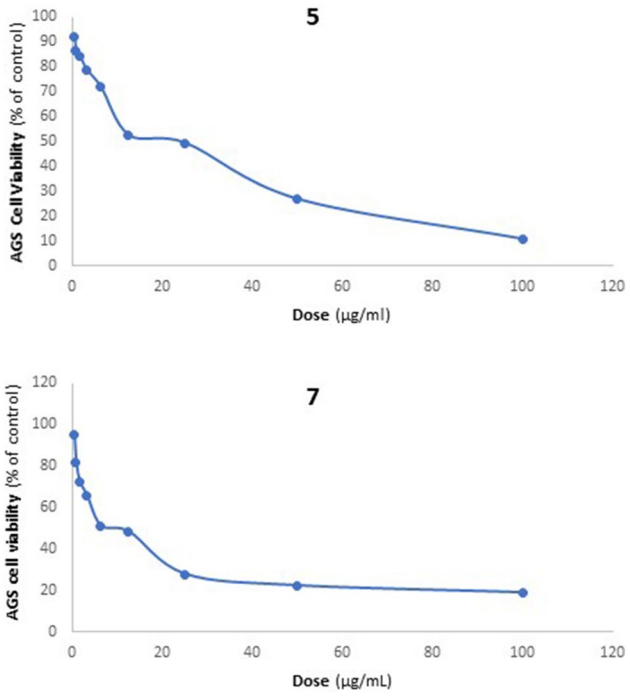

Fig. 2 Percentage of AGS cell viability in different doses of compounds **5** & **7**

Comparison of the obtained cytotoxicity data with previous results on similar DHPM derivatives showed that these compounds were better cytotoxic agents than *N*-phenyl 4-phenyl and *N*-phenyl 4-(3-chlorophenyl) thioxo derivatives but weaker than *N*-phenyl 4-(3-bromophenyl), *N*-phenyl 4-(3-fluorophenyl) and *N*-phenyl 4-(3-phenoxyphenyl) thioxo derivatives against AGS cells [30]. Although not confirmed, cytotoxicity results might have some dependence on lipophilicity and cell penetration. For instance, compounds **4** and **5**, with higher lipophilicities (5.1 and 4.23), showed higher cytotoxicities and fluoro substituent of compound **7** may enhance cellular uptake.

Cell migration inhibitory effect by wound healing assay

As shown in Fig. 3, 24-h post-culturing and treatment of AGS cells with IC_{50} dose of compounds **3**, **4** and **5**, revealed somewhat inhibitory effects on cell migration compared to the control group (untreated cells) and this effect was greater in the case of **4**. However, migration in untreated AGS cells was normal and they were able to largely cover the resulting cell wound. It was interesting to note that compounds **6**–**8** exhibited the excitatory effect on AGS cell migration (Fig. 4) and the effect could be prioritized as **7** > **6** > **8**. The rate of cell wound coverage within compounds **6** and **7** was relatively higher than the control and for **8** was relatively similar to untreated cells even after 48 h. The effect of solvent (DMSO) on wound healing in AGS cells was explored after 24-h culture, and it was revealed that migration in untreated AGS cells (control) and DMSO-treated AGS cells was normal and they were able to largely cover the resulting cell wound (Fig. 5).

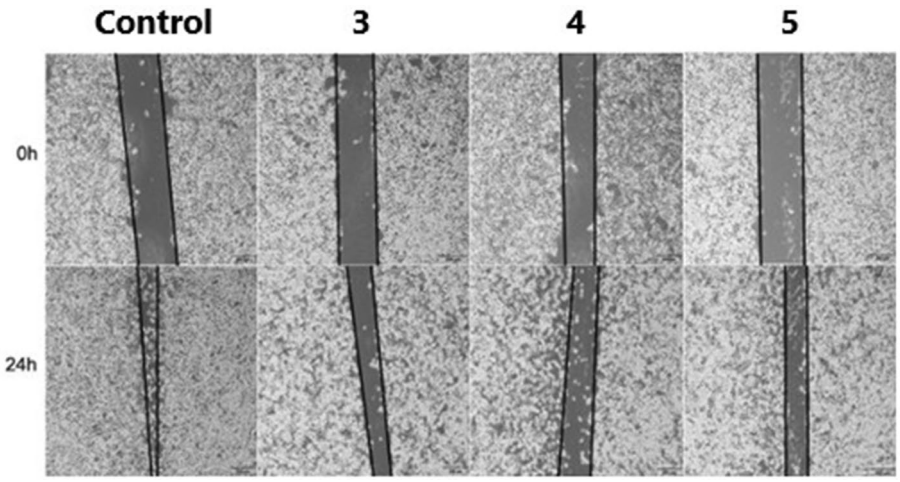

Fig. 3 Effect of synthesized compounds **3**, **4** & **5** on in vitro cell migration behavior of AGS cells. After 24-h culture, AGS cells started to migrate more slowly than the control group. The rate of wound healing in **4**-treated group indicated to be much slower than two other compounds

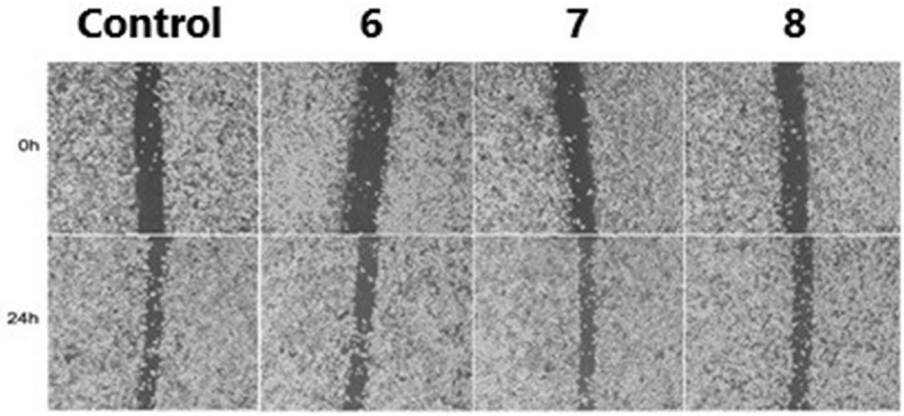

Fig. 4 The effect of synthesized compounds **6**, **7** & **8** on in vitro cell migration behavior of AGS cells. After 24-h culture, in the case of **6** and **7**, AGS cells started to migrate fast with regard to the control and migration rate for **8** was relatively similar to untreated cells

One possible explanation for observed cell migration inhibitory effects would be an apparent difference among the structures of **3**–**5** with **6**–**8** in a way that compounds **3**–**5** included fused benzene ring to the thiazole scaffold, while compounds **6**–**8** were only composed of thiazole rings. At the first glance, such observation directs us toward something like antagonist or agonist effect on a definite cellular site of action for **3**–5 and **6**–**8**, respectively. Although more extensive studies are required to pursue the trend, such findings may be useful in further molecular modifications with the aim of developing more potent inhibitors of cell migration.

Molecular docking

Eg5 is known as a microtubule-dependent motor protein and has been suggested to play an important role in cancer development due to its critical function in the assembly and maintenance of bipolar spindle [19]. Eg5 participates in spindle motions and chromosomes in cell division and affects spindle function through cell localization [32]. Recently, evidence has shown that Eg5 expression

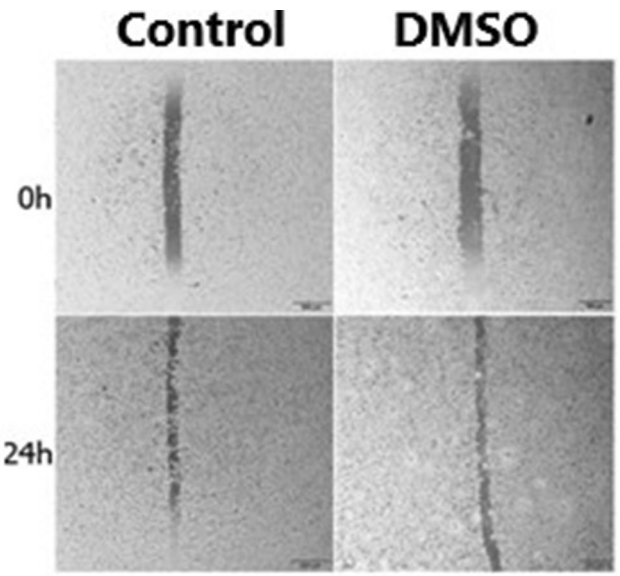

Fig. 5 The effect of DMSO on wound healing in AGS cells in vitro. After 24-h culture, migration in untreated AGS cells (control) and DMSO-treated ones was normal and they were able to largely cover the resulting cell wound

is highly associated with different types of human cancer such as gastric adenocarcinoma [17, 33, 34] and Eg5 inhibitors also show antitumor activity. Studies have shown that Eg5 protein expression was significantly associated with metastasis and TNM stage. Thus, Eg5 is a suitable target for new anticancer therapies in certain types of cancer [35].

In the light of above explanations, we decided to explore the potential binding interactions of assessed compounds within L5/α2/α3 allosteric site of Eg5 as a validated microtubule-dependent target for DHPMs. In order to explore the structural validation of predicted docked poses, initial step was dedicated to the estimation of root mean square deviation (RMSD) of the Cartesian coordinates of re-docked co-crystallographic ligand atoms as a validation criterion. On the basis of re-docking results (Table 2), adaptable predictability levels (≤ 2 Å) could be achieved with 50 independent GA runs and 2.5×10^7 maximum number of evaluations for PDB accession codes 2X7E and 2IEH, but the former was selected to run the simulations for lower value of RMSD.

A validated simulation protocol was applied to dock compounds **3**–**8** into the L5/α2/α3 allosteric site of Eg5 with the aim of selecting top binders. To explain more, L5/α2/α3 allosteric site is a known Eg5 site targeted by inhibitors [36]. Results showed that *R*-configured compound **4** had the highest binding free energy (ΔG_b − 9.52 kcal/mol) (Table 3). To observe the involved Eg5 residues, 3D schematic representation of binding interactions is summarized in Fig. 6 and Table 4.

Results of docking study with regard to binding of DHPMs into Eg5 allosteric site may indicate that:

(1) *S*-enantiomers of DHPMs showed higher binding affinity to Eg5. Monastrol has also been reported to interact to Eg5 in the *S*-configured form [37].

Table 3 AutoDock 4.2 driven free binding energies for different optical isomers of DHPMs under study with Eg5 enzyme binding site (PDB code: **2×7e**)

Ligand molecule	GA Runs	Top-ranked conformational population	ΔG_b (kcal/mol)
R-3	50	8	− 8.04
S-3	50	30	− 9.50
R-4	50	34	− 9.14
***S*-4**	**50**	**35**	**− 9.52**
R-5	50	40	− 8.22
S-5	50	17	− 8.78
R-6	50	21	− 6.88
S-6	50	50	− 7.06
R-7	50	50	− 7.19
S-7	50	50	− 7.44
R-8	50	40	− 7.48
S-8	50	24	− 8.12

The bold value represents the highest achieved docked Gibbs free energy

(2) Binding of top-ranked derivatives (**3**–**5**) could be characterized by dominant hydrophobic pattern (Fig. 6 and Table 4). Several hydrophobic interactions exhibited possible antagonistic behavior in the binding site of Eg5. The issue was reported previously for dihydropyrimidinethione core of monastrol with Gly117, Ile136, Pro137, Tyr211, Leu214, and Ala218 [36].

(3) Structure binding relationship indicated the importance of fused benzene ring in tighter binding of compounds **3**–**5** to Asp896, Tyr211 and Ala133.

(4) Obtained binding data were relatively correlated with cell migration inhibitory results. Compounds **6**–**8** exhibited lower binding energies to Eg5 binding site (ΔG_b − 6.88 to − 8.12 kcal/mol) and fastened the rate of cell wound coverage with regard to untreated

Table 2 AutoDock4.2 validation results for different 3D holo Eg5-ligand complexes retrieved from PDB

No.	PDB code	Resolution (Å)	Co-crystallographic ligand	Top-ranked population (out of 50)	ΔG_b (kcal/mol)	RMSD from reference (Å)
1	2X7E	2.40	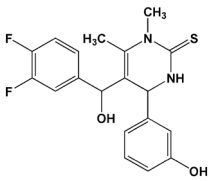	50	− 9.60	1.02
2	2IEH	2.70	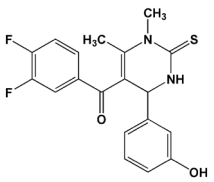	49	− 10.16	1.79

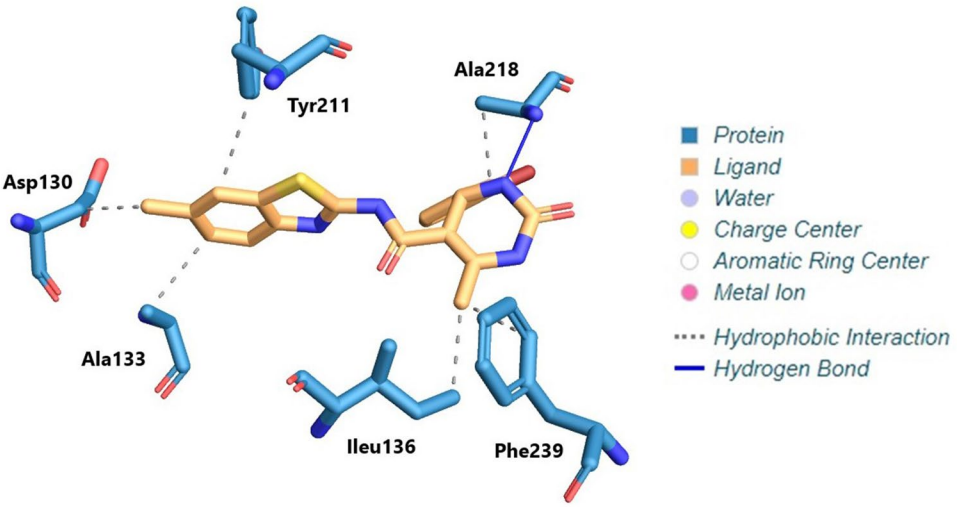

Fig. 6 3D representation of chemical interactions for *S* isomer of compound **4** in binding to Eg5 allosteric binding site (PDB code: **2×7e**)

Table 4 Hydrophobic/H-bond interactions of *S* isomer of compound **4** in binding to the Eg5 enzyme bonding site (PDB code: **2×7e**)

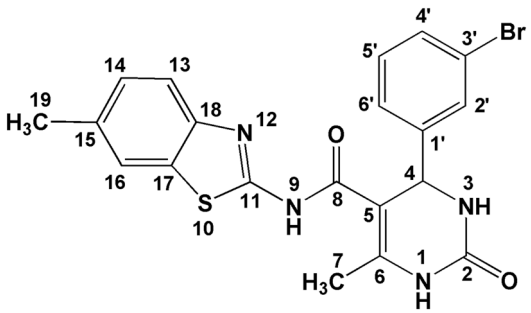

Index	Residue	AA	Distance	Interacted ligand atom/No	Interacted protein atom
1	130A	ASP	3.00	CH_3 (19)	Side chain CH_2
2	133A	ALA	3.47	C (13)	Side chain CH_3
3	136A	ILE	3.04	CH_3 (7)	Side chain CH
4	211A	TYR	3.59	C (16)	Side chain Phenol CH
5	218A	ALA	3.17	C(2′)	Side chain CH_3
w	239A	PHE	3.59	CH_3 (7)	Side chain Phenol CH
7	218A	ALA	2.05	N–H (3)	Backbone N

AGS cells. The case for compounds **3**–**5** (ΔG_b − 8.04 to − 9.52 kcal/mol) was vice versa. However, further biological assessments are required to confirm the proposed relation of treated-cell migration and Eg5 binding ability.

Molecular dynamics

MD simulation is an efficient strategy to improve docking models since flexibility of both ligand and macromolecule are considered during a reasonable run time [38]. To evaluate the stability of predicted Eg5 complex with regard to the dynamic characteristics of the protein, 50 ns MD simulation of Eg5 was conducted in the presence of top-ranked docked ligand ***S*-4** in explicit water. The stability of Eg5 during simulation was assessed via monitoring root mean square deviation (RMSD), root mean square fluctuations (RMSF) and radius of gyration (Rg). Moreover; to compare the MD results with the reference compound, MD of the co-crystallographic *R*-fluorastrol and Eg5 complex was also performed.

Approximate leveling-off in deviation from primary Eg5 structure was gradually achieved after 10 ns of simulation indicating that the system folded to a more stable conformation with regard to the starting structure (Fig. 7). The low RMSD value of the complex revealed the stable binding of ***S*-4** to Eg5 and indicated the convergence of Eg5 to equilibrium structure (Average RMSD 2.75 Å). Besides protein backbone RMSD, the stability of docked complex must also be inferred in terms of ligand fluctuations. For this purpose, the RMSD of all atoms of compound ***S*-4** was estimated and is shown in Fig. 7. It was found that the RMSD profile of the interacted ligand is probably stable with regard to the formed complex (Average RMSD 1.59 Å).

For comparison purposes, RMSD plot for a co-crystallographic ligand *R*-fluorastrol and Eg5 complex during 50 ns was also obtained (Fig. 8). The good RMSD value of the reference complex structure (Average RMSD 2.77 Å). revealed the stable binding of the cognate ligand to Eg5 binding site for 50 ns, and moreover the average RMSD variations of the cognate ligand were found to be 1.86 Å. Relatively similar

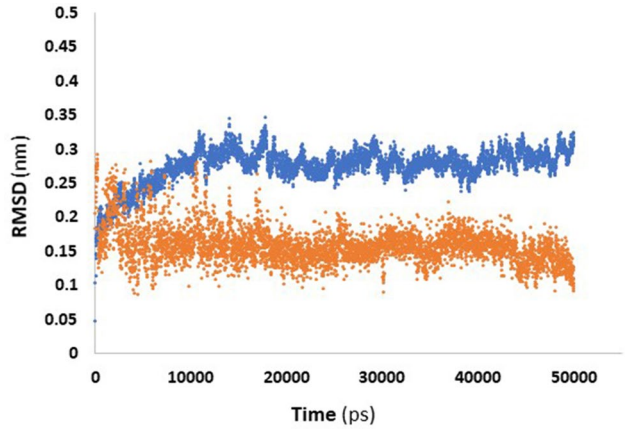

Fig. 7 RMSDs of the backbone atoms of Eg5 (up) and all atoms of compound ***S*-4** (down) during MD simulations (0–50 ns)

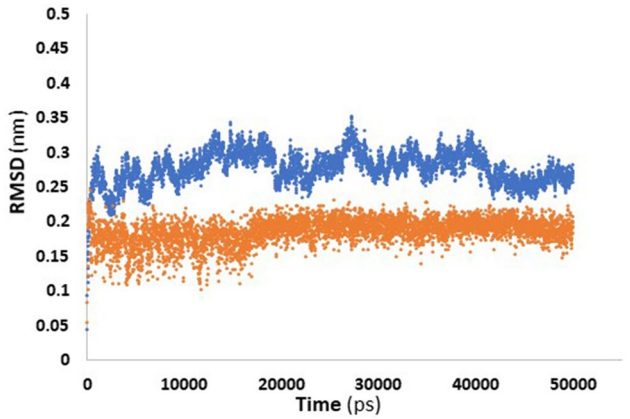

Fig. 8 RMSDs of the backbone atoms of Eg5 (up) and all atoms of a co-crystallographic ligand *R*-fluorastrol (down) during MD simulations (0–50 ns)

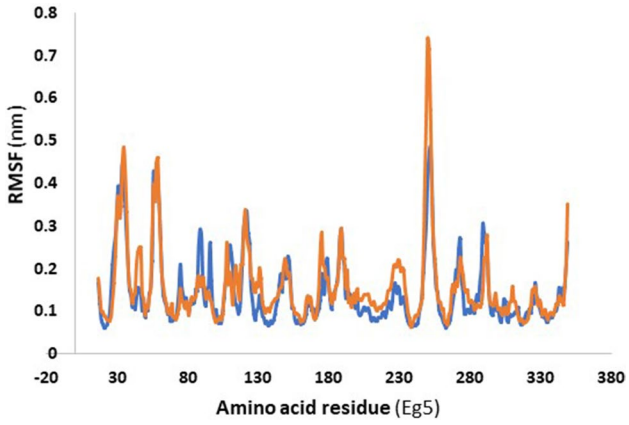

Fig. 9 RMSF of the backbone atoms of Eg5 in complex with *S*-4 (blue) and *R*-fluorastrol (orange) during MD simulations (0–50 ns)

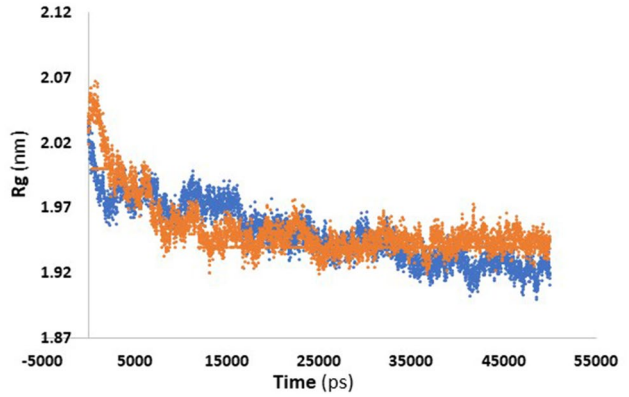

Fig. 10 Time dependence of the radius of gyration (Rg) graph of Eg5 in complex with *S*-4 (blue) and *R*-fluorastrol (orange) during MD simulations (0–50 ns)

trend could be observed for reference macromolecule structure since at about 10 ns, but after a less steep slope the equilibrium state could be achieved. Although the whole RMSD variation for *R*-fluorastrol was desirable, after about 15 ns a very stable binding trajectories were attained p to the end of MD simulations which is indicative of a stable binding mode toward Eg5 allosteric site. In the case of docked ligand, although average RMSD during 50 ns was even less than the cognate ligand and very desirable, particularly initial 10 ns of the MD simulation was accompanied by more conformational fluctuations. One of the interesting outcomes of RMSD plots was appropriate compatibility of corresponding conformational fluctuations between ligand and protein within both RMSD plots.

Average atomic mobility of the Eg5 Cα atoms is indicative of the flexibility of individual residues within the MD simulations and can be estimated through RMSF calculation (Fig. 9). Conformational changes of the interacted residues were all very small, and main fluctuations (> 0.3 nm) occurred to residues far from ligand binding site. To explain more, RMSF variations for co-crystallographic and docked complexes were found to be 0.15 and 0.14 nm, respectively. Ile250 (RMSF 0.74 nm) of co-crystallographic complex and Glu253 (RMSF 0.37 nm) of docked complex were the only amino acid residues with significant RMSF values. In the case of Ser75, Pr088, Ile89, Asp91, Gly96 and Tyr97 the docked RMDF was significantly more than a corresponding residue in co-crystallographic complex. The narrow range of estimated RMSFs for binding site residues confirmed the RMSD results and demonstrated the capability of ***S*-4** to form stable interactions with Eg5 during MD simulation.

The compactness of Eg5 was evaluated by radius of gyration (Rg) (Fig. 10). It was found that residual backbones and folding of Eg5 were consistently stable after binding to ***S*-4** and *R*-fluorastrol. The Rg of the backbone atoms of Eg5 was decreased from about 2.05 nm at the beginning to

about 1.94 nm after 12.5 ns in the presence of *R*-fluorastrol and 1.92 nm after 30 ns in the presence of ***S*-4**. Moreover, Rg plot showed that the decrease in Rg was associated with steeper slope during the initial 3 ns of simulation. Results indicated that compound ***S*-4** was able to potentially induce desirable compact structure of Eg5 (Fig. 10).

To explore the stability of binding interactions, it was decided to achieve the complex structure after 50 ns and as is depicted in Fig. 11, Ala218 was the sole residue with conserved H-bond interaction via backbone N and N3H of ligand. Conformational fluctuation of the system during 50 ns provided a new hydrogen bond between Leu214 backbone N and N3-H of ligand. In this regard, the HBD group N3H of the DHPM ring seemed to be an important site of action for this compound. A few amino acid residues changed their attitude toward ligand and participated in hydrophobic contacts to the carbon skeleton of the docked complex. Besides H-bond interaction, Ala218 also made a hydrophobic contact via side chain methyl to the *ortho* carbon atom of bromophenyl moiety. Tyr211, Phe239 and Ala133 could not be detected for the stable complex after 50 ns MD simulation.

Conclusion

DHPM derivative (**4**) with 4-(*3*-bromo phenyl) substituent showed the greatest inhibitory effect of AGS cell migration, probably due to its bulkier nature and higher hydrophobicity (Table 1). In contrast to 4, DHPMs that possessed thiazole but not benzothiazole ring exhibited no inhibitory effect on in vitro cell migration of AGS cells indicating a determinant role of phenyl ring of benzothiazole in detected inhibitory effects of *N*-(benzothiazol-2-yl)-5-carboxamide derivatives. MD simulations of top-ranked docked pose of compound **4** showed that RMSD of ligand-receptor complex inclined to converge, representing that the systems evolved into stable and equilibrated states. It was interesting to note that improved polar interactions were probably driving force for re-orientation of compound **4** in the binding site of Eg5 to achieve more stable binding mode. Results of this study prompt us to perform further structural modification of the assessed compounds and achieve DHPM derivatives that possess superior effects in preventing the migration of AGS cancer cells.

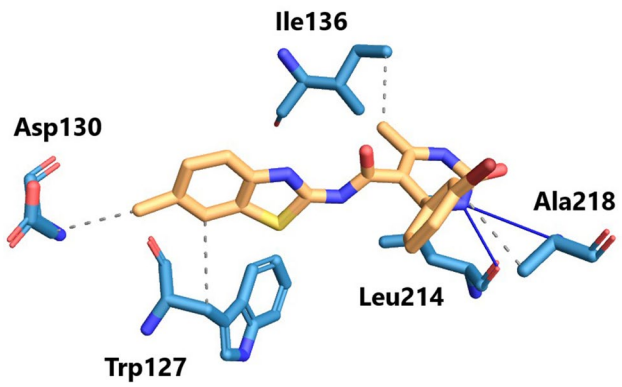

Fig. 11 3D representation of chemical interactions for *S* isomer of compound **4** in binding to Eg5 allosteric binding site (PDB code: **2×7e**) after 50-ns MD simulations

Supplementary material

The spectra (actual analytical data) of the newly synthesized compounds are accessible in Supplementary Materials.

Supplementary Information The online version contains supplementary material available at https://doi.org/10.1007/s11030-021-10229-z.

Acknowledgements The research leading to offered results received funding from Ardabil University of Medical Sciences (ARUMS) under Grant No. IR.ARUMS.REC.1398.259.

Authors' contributions All authors contributed equally in this work (concept, design, definition of intellectual content, literature search, experimental studies, data acquisition, data analysis, statistical analysis, manuscript preparation, manuscript editing and manuscript review).

Funding The research leading to offered results received funding from Ardabil University of Medical Sciences (ARUMS) under Grant No. IR.ARUMS.REC.1397.137.

Availability of data and material All the data are available and can be offered on request.

Code availability Not applicable.

Declaration

Conflict of interest Authors declare to have no conflicts of interests.

References

1. Pecorino L (2016) Molecular biology of cancer: mechanisms, targets, and therapeutics. Oxford University Press, New York
2. Mons U, Gredner T, Behrens G, Stock C, Brenner H (2018) Cancers due to smoking and high alcohol consumption. Dtsch Arztebl Int 115(35–36):571–577
3. Hartgrink HH, Jansen EP, van Grieken NC, van de Velde CJ (2009) Gastric cancer. Lancet 374(9688):477–490
4. Jiang F, Shen X (2019) Current prevalence status of gastric cancer and recent studies on the roles of circular RNAs and methods used to investigate circular RNAs. Cell Mol Biol Lett 24:53
5. Seyfried TN, Huysentruyt LC (2013) On the origin of cancer metastasis. Crit Rev Oncog 18(1–2):43–73

6. Kobayashi H, Enomoto A, Woods SL, Burt AD, Takahashi M, Worthley DL (2019) Cancer-associated fibroblasts in gastrointestinal cancer. Nat Rev Gastroenter Hepatol 16(5):282–295
7. Alberts S, Cervantes A, Van de Velde C (2003) Gastric cancer: epidemiology, pathology and treatment. Ann Onc 14:ii31–ii36
8. Wang F, Li T, Zhang B, Li H, Wu Q, Yang L, Nie Y, Wu K, Shi Y, Fan D (2013) MicroRNA-19a/b regulates multidrug resistance in human gastric cancer cells by targeting PTEN. Biochem Biophys Res Com 434(3):688–694
9. Bidram Z, Sirous H, Khodarahmi GA, Hassanzadeh F, Dana N, Hariri AA, Rostami M (2020) Monastrol derivatives: in silico and in vitro cytotoxicity assessments. Res Pharm Sci 15(3):249–262
10. Sawin KE, LeGuellec K, Philippe M, Mitchison TJ (1992) Mitotic spindle organization by a plus-end-directed microtubule motor. Nature 359(6395):540–543
11. Pérez-Melero C (2014) KSP inhibitors as antimitotic agents. Curr Top Med Chem 14(20):2286–2311
12. Luo L, Carson JD, Dhanak D, Jackson JR, Huang PS, Lee Y, Sakowicz R, Copeland RA (2004) Mechanism of inhibition of human KSP by monastrol: insights from kinetic analysis and the effect of ionic strength on KSP inhibition. Biochemistry 43(48):15258–15266
13. González-Hernández E, Aparicio R, Garayoa M, Montero MJ, Sevilla MÁ, Pérez-Melero C (2019) Dihydropyrimidine-2-thiones as Eg5 inhibitors and L-type calcium channel blockers: potential antitumour dual agents. MedChemComm 10(9):1589–1598
14. Nakai R, Iida S, Takahashi T, Tsujita T, Okamoto S, Takada C, Akasaka K, Ichikawa S, Ishida H, Kusaka H, Akinaga S, Murakata C, Honda S, Nitta M, Saya H, Yamashita Y (2009) K858, a novel inhibitor of mitotic kinesin Eg5 and antitumor agent, induces cell death in cancer cells. Cancer Res 69(9):3901–3909
15. Khathi SP, Chandrasekaran B, Karunanidhi S, Tham CL, Kozielski F, Sayyad N, Karpoormath R (2018) Design and synthesis of novel thiadiazole-thiazolone hybrids as potential inhibitors of the human mitotic kinesin Eg5. Bioorg Med Chem Lett 28(17):2930–2938
16. Van Meerloo J, Kaspers GJ, Cloos J (2011) Cell sensitivity assays: the MTT assay. In: Cancer cell culture, Humana Press
17. Sun XD, Shi XJ, Sun XO, Luo YG, Wu XJ, Yao CF, Yu HY, Li DW, Liu M, Zhou J (2011) Dimethylenastron suppresses human pancreatic cancer cell migration and invasion in vitro via allosteric inhibition of mitotic kinesin Eg5. Acta Pharm Sin 32(12):1543
18. Wang X, Decker CC, Zechner L, Krstin S, Wink M (2019) In vitro wound healing of tumor cells: inhibition of cell migration by selected cytotoxic alkaloids. BMC Pharm Toxic 20(1):1–2
19. Morris G, Huey R, Lindstrom W, Sanner MF, Belew RK, Goodsell DS, Olson AJ (2009) AutoDock4 and AutoDockTools4: automated docking with selective receptor flexibility. J Comput Chem 30(16):2785–2791
20. Sanner M (1999) Python: a programming language for software integration and development. J Mol Graph Model 17(1):57–61
21. Razzaghi-Asl N, Ebadi A, Shahabipour S, Gholamin D (2020) Identification of a potential SARS-CoV2 inhibitor via molecular dynamics simulations and amino acid decomposition analysis. J Biomol Struct Dyn. https://doi.org/10.1080/07391102.2020.1797536
22. Salentin S, Schreiber S, Haupt VJ, Adasme MF, Schroeder M (2015) PLIP: Fully automated protein-ligand interaction profiler. Nucleic Acids Res 43(W1):W443–W447
23. Kaan HYK, Ulaganathan V, Rath O, Prokopcova H, Dallinger D, Kappe CO, Kozielski F (2010) Structural basis for inhibition of Eg5 by dihydropyrimidines: stereoselectivity of antimitotic inhibitors enastron, dimethylenastron and fluorastrol. J Med Chem 53:5676–5683
24. Spoel VDD, Lindahl E, Hess B, Groenhof G, Mark AE, Berendsen HJ (2005) GROMACS: fast, flexible, and free. J Comput Chem 26:1701–1718
25. Schuttelkopf AW, Aalten DMF (2004) PRODRG: a tool for high-throughput crystallography of protein-ligand complexes. Acta Crystallogr D Biol Crystallogr 60(8):1355–1356
26. Parrinello M, Rahman A (1981) Polymorphic transitions in single crystals: A new molecular dynamics method. J Appl Phys 52(12):7182–7190
27. Hess B, Bekker H, Berendsen HJC, Fraaije J (1997) LINCS: a linear constraint solver for molecular simulations. J Comput Chem 18:1463–1472
28. Darden T, York D, Pedersen L (1993) Particle mesh Ewald: An N log (N) method for Ewald sums in large systems. J Chem Phys 98(12):10089–10092
29. Razzaghi-Asl N, Mirzayi S, Mahnam K, Sepehri S (2018) Identification of COX-2 inhibitors via structure-based virtual screening and molecular dynamics simulation. J Mol Graph Model 83:138–152
30. Bohlooli S, Nejatkhah N, Sepehri S, Doostkamel D, Razzaghi-Asl N (2020) Synthesis and cytotoxicity evaluation of novel cyclic/noncyclic *N*-heteroaryl enamino amides *vs* human cancer cell lines. Res Pharm Sci 15(6):563–570
31. Daina A, Michielin O, Zoete V (2017) SwissADME: a free web tool to evaluate pharmacokinetics, drug-likeness and medicinal chemistry friendliness of small molecules. Sci Rep 7:42717
32. Kapitein LC, Peterman EJG, Kwok BH, Kim JH, Kapoor TM, Schmidt CF (2005) The bipolar mitotic kinesin Eg5 moves on both microtubules that it crosslinks. Nature 435(7038):114–118
33. Sakowicz R, Finer JT, Beraud C, Crompton A, Lewis E, Fritsch A, Lee Y, Mak J, Moody R, Turincio R, Chabala JC, Gonzales P, Roth S, Weitman S, Wood KW (2004) Antitumor activity of a kinesin inhibitor. Cancer Res 64(9):3276–3280
34. Imai T, Oue N, Nishioka M, Mukai S, Oshima T, Sakamoto N, Sentani K, Matsusaki K, Yoshida K, Yasui W (2017) Overexpression of KIF11 in gastric cancer with intestinal mucin phenotype. Pathobiology 84:16–24
35. Lu M, Zhu H, Wang X, Zhang D, Xiong L, Xu L, You Y (2016) The prognostic role of Eg5 expression in laryngeal squamous cell carcinoma. Pathology 48(3):214–218
36. Myers SM, Collins I (2016) Recent findings and future directions for interpolar mitotic kinesin inhibitors in cancer therapy. Future Med Chem 8(4):463–489
37. Garcia-Saez I, DeBonis S, Lopez R, Trucco F, Rousseau B, Thuery P, Kozielski F (2007) Structure of human Eg5 in complex with a new monastrol-based inhibitor bound in the R configuration. J Biol Chem 282:9740–9747
38. Durrant JD, McCammon JA (2011) Molecular dynamics simulations and drug discovery. BMC Biol 9:71–79

Authors and Affiliations

Mohsen Sagha[1] · Fatemeh Mousaei[2] · Mahtab Salahi[2] · Nima Razzaghi-Asl[3]

✉ Nima Razzaghi-Asl
n.razzaghi@pharmacy.arums.ac.ir

[1] Research Laboratory for Embryology and Stem Cells, Department of Anatomical Sciences, School of Medicine, Ardabil University of Medical Sciences, Ardabil, Iran

[2] Student Research Committee, School of Pharmacy, Ardabil University of Medical Sciences, Ardabil, Iran

[3] Department of Medicinal Chemistry, School of Pharmacy, Ardabil University of Medical Sciences, 5618953141 Ardabil, Iran